The Astrophysical Journal, 848:80 (8pp), 2017 October 20 https://doi.org/10.3847/1538-4357/aa8d15

NuSTAR Hard X-Ray Observation of the Gamma-Ray Binary Candidate HESS J1832–093

Kaya Mori[1], E. V. Gotthelf[1], Charles J. Hailey[1], Ben J. Hord[1], Emma de Oña Wilhelmi[2], Farid Rahoui[3,4], John A. Tomsick[5], Shuo Zhang[6], Jaesub Hong[4], Amani M. Garvin[1], Steven E. Boggs[5], Finn E. Christensen[7], William W. Craig[5,8], Fiona A. Harrison[9], Daniel Stern[10], and William W. Zhang[11]
[1] Columbia Astrophysics Laboratory, Columbia University, New York, NY 10027, USA
[2] Institute of Space Sciences (CSIC-IEEC), E-08193 Barcelona, Spain
[3] European Southern Observatory, K. Schwarzschild-Strasse 2, D-85748 Garching bei München, Germany
[4] Harvard-Smithsonian Center for Astrophysics, Cambridge, MA 02138, USA
[5] Space Sciences Laboratory, University of California, Berkeley, CA 94720, USA
[6] Kavli Institute for Astrophysics and Space Research, Massachusetts Institute of Technology, Cambridge, MA 02139, USA
[7] DTU Space—National Space Institute, Technical University of Denmark, Elektrovej 327, DK-2800 Lyngby, Denmark
[8] Lawrence Livermore National Laboratory, Livermore, CA 94550, USA
[9] Cahill Center for Astronomy and Astrophysics, California Institute of Technology, Pasadena, CA 91125, USA
[10] Jet Propulsion Laboratory, California Institute of Technology, Pasadena, CA 91109, USA
[11] NASA Goddard Space Flight Center, Greenbelt, MD 20771, USA
Received 2017 June 16; revised 2017 August 19; accepted 2017 September 12; published 2017 October 13

Abstract

We present a hard X-ray observation of the TeV gamma-ray binary candidate HESS J1832−093, which is coincident with the supernova remnant G22.7−0.2, using the *Nuclear Spectroscopic Telescope Array*. Non-thermal X-ray emission from XMMU J183245−0921539, the X-ray source associated with HESS J1832−093, is detected up to ∼30 keV and is well-described by an absorbed power-law model with a best-fit photon index $\Gamma = 1.5 \pm 0.1$. A re-analysis of archival *Chandra* and *XMM-Newton* data finds that the long-term X-ray flux increase of XMMU J183245−0921539 is 50^{+40}_{-20}% (90% C.L.), much less than previously reported. A search for a pulsar spin period or binary orbit modulation yields no significant signal to a pulse fraction limit of $f_p < 19\%$ in the range 4 ms $< P <$ 40 ks. No red noise is detected in the FFT power spectrum to suggest active accretion from a binary system. While further evidence is required, we argue that the X-ray and gamma-ray properties of XMMU J183245−0921539 are most consistent with a non-accreting binary generating synchrotron X-rays from particle acceleration in the shock formed as a result of the pulsar and stellar wind collision. We also report on three nearby hard X-ray sources, one of which may be associated with diffuse emission from a fast-moving supernova fragment interacting with a dense molecular cloud.

Key words: gamma rays: general – radiation mechanisms: non-thermal – X-rays: binaries

1. Introduction

High-energy gamma-ray surveys using ground-based Cherenkov telescopes (e.g., MAGIC, H.E.S.S, and VERITAS) have uncovered a rare subclass of TeV binary systems (Dubus 2013, 2015). Whereas the majority of the ∼80 identified Galactic TeV sources are associated with either pulsar wind nebulae (PWNe) or supernova remnants (SNRs), six gamma-ray binaries have been detected above $E \sim 100$ GeV. These include PSR B1259-63, LS 5039, LS I +61 303, HESS J0632+057, 1FGL J1018.6−5856, and most recently PSR J2032+4127 (Aharonian et al. 2005, 2006, 2007; Albert et al. 2009; H.E.S.S. Collaboration et al. 2015; Lyne et al. 2015). These sources are all identified as non-accreting binaries harboring an O or B main-sequence star and a compact object, with a wide range of orbital periods from 3.9 days to ∼50 years. With the exception of PSR B1259−63 and PSR J2032+4127, both of which are known to have radio pulsars, the nature of the compact object, whether a neutron star (NS) or black hole (BH), remains unknown.

Gamma-ray emission from TeV binaries is generally thought to originate from particle acceleration in the shock formed between the stellar wind and the pulsar wind (Tavani et al. 1994; Sierpowska-Bartosik & Torres 2008; Dubus 2013). Both X-rays and gamma-rays result from synchrotron and inverse Compton scattering in the interaction region, respectively, and show a strong dependence on orbital phase. Other scenarios such as the microquasar model (Romero et al. 2003; Bosch-Ramon & Paredes 2004) are less plausible since the spectral and timing properties are similar in all TeV gamma-ray binaries, including the two containing radio pulsars (Dubus 2013). Multi-wavelength monitoring of the gamma-ray binaries in the X-ray, GeV, and TeV bands revealed the complex emission mechanisms and geometry (Kaspi et al. 1995; Chernyakova et al. 2006a, 2006b, 2009; Kishishita et al. 2009; Takahashi et al. 2009; Uchiyama et al. 2009; Li et al. 2011; Rea & Torres 2011; An et al. 2013, 2015; Aliu et al. 2014; Ho et al. 2017). A number of theoretical models, including numerical hydrodynamics simulations, have been developed to account for the orbital dependence of the X-ray and gamma-ray spectra via anisotropic radiation processes, relativistic Doppler boosting, and inhomogeneous stellar winds (Dubus et al. 2015; de la Cita et al. 2017; Takata et al. 2017). Studying these rare gamma-ray binaries not only probes the unique environment of the pulsar and stellar wind interaction but also sheds light on the (short) X-ray binary evolution stage before they become "regular" accretion powered high-mass X-ray binaries (HMXBs; Dubus 2013).

The unresolved TeV point source HESS J1832−093 was discovered in the vicinity of SNR G22.7−0.2, suggesting a

possible association (Abramowski et al. 2015). However, follow-up X-ray observations favored a binary origin for the TeV emission (Eger et al. 2016). The bright X-ray source XMMU J183245−0921539 (XMMJ183245 herein) lies within the gamma-ray error circle (Abramowski et al. 2015) and is associated with a *Chandra* point source (Eger et al. 2016). The latter authors reported a large factor of 4 increase in the *Chandra* flux relative to the earlier *XMM-Newton* measurement that seemed to rule out the PWN or SNR scenario for the X-rays. Instead, the coincidence of a bright IR source at the *Chandra* coordinates, a plausible counterpart, suggests a binary scenario for powering the gamma-ray emission (Eger et al. 2016).

In this paper, we present a *NuSTAR* X-ray observation of the field containing HESS J1832−093, along with a re-analysis of the archival *XMM-Newton* and *Chandra* data. Observational details of these data sets are given in Section 2. Spectroscopy and timing results on XMMJ183245 are reported in Section 3 and Section 4, respectively. Our analysis of archival *Chandra* data refutes reports in previous work of large flux variations. Nevertheless, we find sufficient evidence to prefer the TeV gamma-ray binary scenario for HESS J1832−093. A timing analysis detailed in Section 4 places upper limits on any probable pulsar or binary signal. We also present the analysis, in Section 5, of three nearby hard X-ray sources. We discuss the nature of HESS J1832−093 and the hard sources in Section 6. Finally, we summarize our results in Section 7.

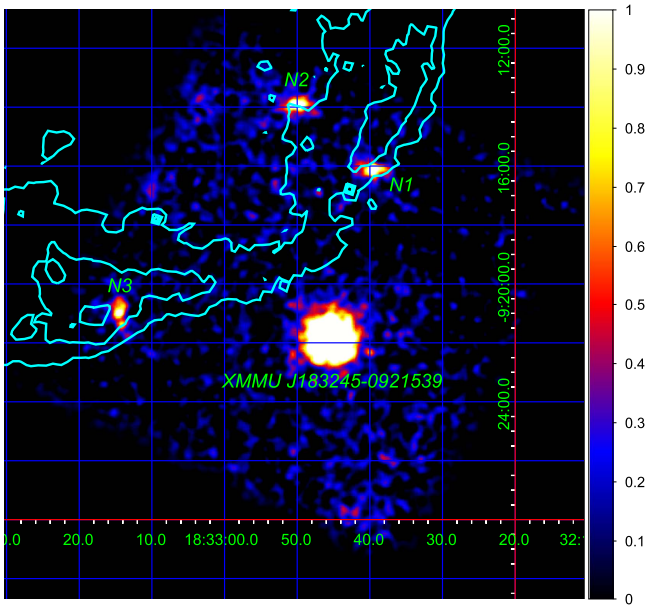

Figure 1. Background-subtracted *NuSTAR* 3-30 keV image overlaid with 20 cm radio (cyan) contours of the SNR shell G22.7−0.2 (Helfand et al. 2006). We combined module A and B images after subtracting background models generated by `nuskybgd`. The image was smoothed by a Gaussian kernel with a 5-pixel (12.″5) width. The image shows the X-ray counterpart of HESS J1832−093 and three other X-ray sources (N1, N2, and N3).

2. *NuSTAR* Observation and Data Reduction

An 87 ks *NuSTAR* observation of the field containing HESS J1832−093 was obtained on 2016 March 21 as part of the *NuSTAR* TeV survey project. *NuSTAR* consists of two co-aligned X-ray telescopes, with corresponding focal plane modules FPMA and FPMB that provide 18″ FWHM imaging resolution over a 3–79 keV X-ray band, with a characteristic spectral resolution of 400 eV FWHM at 10 keV (Harrison et al. 2013). The reconstructed *NuSTAR* coordinates are accurate to 7.″5 at the 90% confidence level. The nominal timing accuracy of *NuSTAR* is ∼2 ms rms, after correcting for drift of the on-board clock, with the absolute timescale shown to be better than <3 ms (Mori et al. 2014; Madsen et al. 2015).

The data were processed and analyzed using the `FTOOLS` 09May2016_V6.19 software package including `NUSTARDAS` 14Apr16_V1.6.0, with *NuSTAR* Calibration Database (CALDB) files from 2016 July 6. No flares were evident during the observation, resulting in a total of 86.9 ks of net usable exposure times spanning 171.5 ks. For all following spectral analysis, extracted spectra, grouped into appropriate channels, were fitted using the `XSPEC` (v12.8.2) package (Arnaud et al. 1996). These fits make use of the `TBabs` absorption model in `XSPEC` with the `wilm` solar abundances (Wilms et al. 2000) and the `vern` photoionization cross-section (Verner et al. 1996). χ^2 statistics were used to evaluate the spectral fits. All errors quoted herein are for the 90% confidence level (C.L.).

The *NuSTAR* background contamination is highly variable across the focal plane of the two FPM detectors. We use the `nuskybgd` software (Wik et al. 2014) to help model the spatial and energy-dependent cosmic X-rays and a detector background. This allows us to generate, for each detector, a model energy-resolved background map for image analysis and background spectra at the source location for our spectral analysis. The background model components are normalized by simultaneously fitting *NuSTAR* spectra in three source-free regions. The `nuskybgd` model fit to the source-free spectra yields $\chi^2_\nu = 1.1$ (1472 dof) without apparent Fe lines at E ∼6–7 keV, which is indicative of the Galactic ridge X-ray emission (Mori et al. 2015). In addition, as shown in Section 3, *NuSTAR* module A and B spectra of the brightest X-ray source in the FOV (XMMJ183245) jointly fit by an absorbed power-law model show that their relative flux normalization is 2%. The 2% flux discrepancy between the two module spectra is not only below the statistical errors (∼3%) but also it indicates that any additional background component unaccounted for by the `nuskybgd` model has a negligible contribution of less than 2% in the 3–30 keV band where all our imaging and spectral analyses are performed.

Figure 1 presents the combined background-subtracted, exposure-corrected, smoothed *NuSTAR* images from the two detector modules, in the 3−30 keV energy band. Using `wavdetect`, we detected four >3σ sources, including the X-ray counterpart XMMJ183245 to HESS J1832−093. Interestingly, the other three *NuSTAR* sources (N1, N2, and N3 hereafter), all of which have *XMM-Newton* counterparts, overlap with the radio shell of SNR G22.7−0.2 (see Figure 1, cyan contours). Above 20 keV, only XMMJ183245 is visible in the *NuSTAR* images (see Figure 2 for two-color *NuSTAR* images in the 10–20 and 20–30 keV bands). Based on the 3XMM source catalog (Rosen et al. 2016), we found that the four *NuSTAR* sources are the brightest among about a dozen *XMM-Newton* point sources in the *NuSTAR* field of view.

We also analyzed archival *XMM-Newton* and *Chandra* observations of the HESS J1832−093 field. A 17 ks *XMM-Newton* exposure (ObsID #0654480101) was obtained on 2011 March 13 and an 18 ks *Chandra* pointing (ObsID #16737) was acquired on 2015 July 6. Details of these observations and their analysis can be found in Abramowski et al. (2015) and

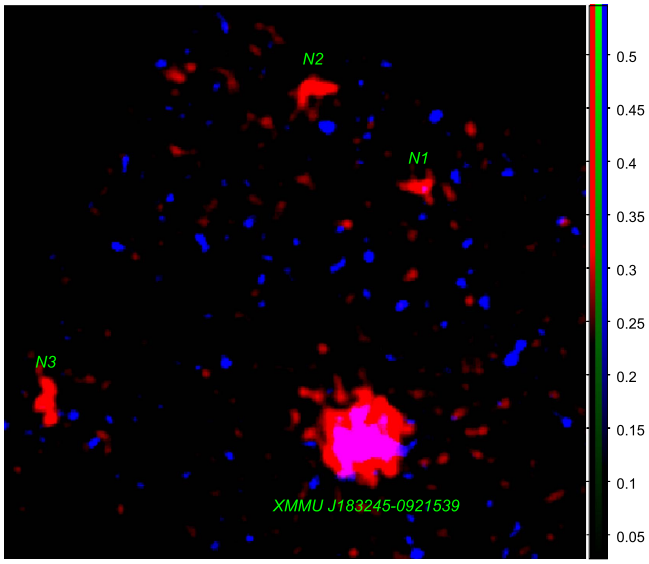

Figure 2. Two-color *NuSTAR* images in 10–20 (red) and 20–30 (blue) keV bands. We combined module A and B images after subtracting background models generated by `nuskybgd` and smoothing by a Gaussian kernel with a 5-pixel (12.″5) width. The image was zoomed-in on the X-ray counterpart of HESS J1832−093 and three other X-ray sources (N1, N2, and N3).

Eger et al. (2016), respectively. Although *Swift* observations overlap with the vicinity, their short exposures result in few photons (15–26 cts) to measure a flux accurately. As reported in Eger et al. (2016), these data suggest no evidence of large flux variability among four data sets spanning 2008 February 28 to 2015 September 26.

3. Spectral Analysis of XMMU J183245−0921539

We extracted *NuSTAR* spectra of XMMJ183245 from a $r = 50''$ region and generated a *NuSTAR* response matrix and ancillary response files using nuproducts. We created a model background spectrum for each of the source regions using the `nuskybgd` tool. As a result, the flux normalization for spectra extracted from the two modules match within 2% of each other. These spectra are grouped with at least 30 counts in each fitted channel bin.

The *NuSTAR* spectra of XMMJ183245 extend up to 30 keV, above which the background dominates, and is well-fit to an absorbed power-law model (Figure 3, top panel). However, the column density derived from these data is found to be unconstrained, with 100% uncertainties. This is also the case for individual fits to the *Chandra* and *NuSTAR* data on XMMJ183245. Instead, for all subsequent spectral fits to individual data sets, we hold the column density fixed to $N_{\rm H} = 9.5 \times 10^{22}\,{\rm cm}^{-2}$. This value results from a simultaneous fit to the *NuSTAR*, *XMM-Newton*, and *Chandra* spectra, as described in the next section (Figure 3, bottom panel). For this nominal column density we obtain a best-fit photon index of $\Gamma = 1.5 \pm 0.1$ for the *NuSTAR* spectra, with a fit statistic of $\chi^2_\nu = 1.0$ (151 dof). This yields an absorbed 2−10 keV flux of $F = 9.6 \pm 0.8 \times 10^{-13}$ erg cm^{-2} s^{-1} for the FPMA spectrum and similar results for the other module. No significant spectral break or cutoff was detected. A summary of all the spectral results for XMMJ183245 obtained herein is given in Table 1.

To explore flux and spectral variations of XMMJ183245 on short timescales (∼6 hr), we repeated our spectral fits to

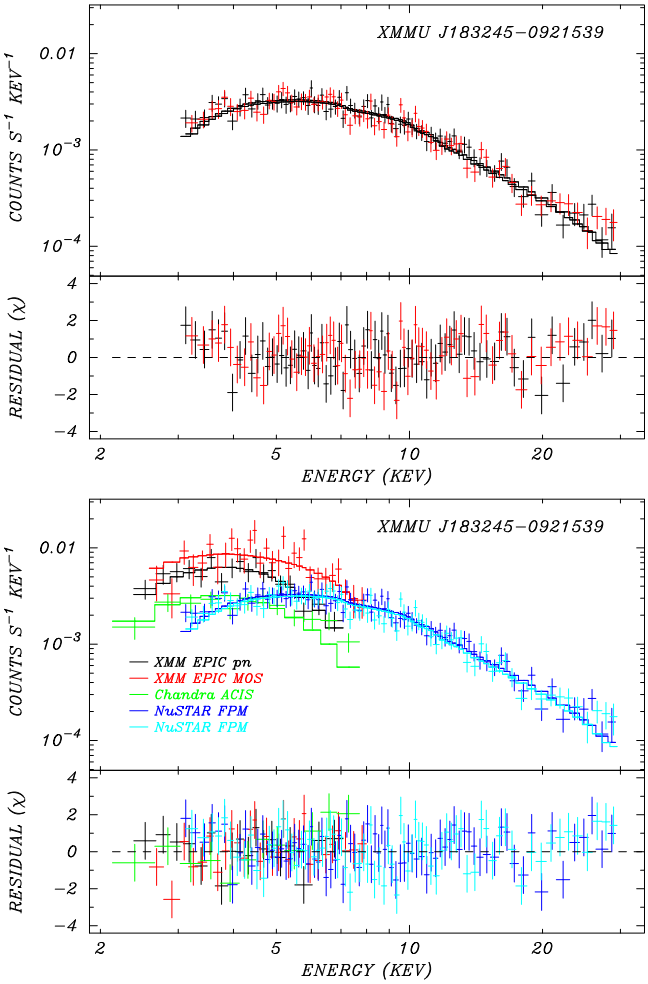

Figure 3. Top: the *NuSTAR* 3–30 keV X-ray spectrum of XMMJ183245 fitted with an absorbed power-law model. The best-fit model (histogram) and data points (crosses) are shown in the top panel. Residuals from the best-fit model are shown in the lower panel. Bottom: simultaneous fit to *Chandra*, *XMM-Newton*, and *NuSTAR* spectra of XMMJ183245, with the column density and power-law index parameters linked. The fitted model is given in Table 1.

NuSTAR data extracted from four equally divided intervals of the light curve (20 ks each) in the 3−30 keV energy range. However, no significant change is found in the flux or photon index during the observation. A similar result is obtained for spectra in the 10−30 keV bands, where any effects of low-energy absorption are expected to be negligible. We conclude that there was no spectral variation during the *NuSTAR* observation to the limit of measurement uncertainties.

To quantify the long-term flux and spectral variability of XMMJ183245 we compare the results of our *NuSTAR* observations with the archival *XMM-Newton* and *Chandra* data sets spanning a total of 5 years. For each mission, we follow the standard reduction and analysis procedures. For *Chandra*, we used the `specextract` script to extract ACIS source counts from a $r < 3''.5$ region file and to generate the spectrum and its response files for the point source. We fit the resulting spectrum to the absorbed power-law model with the column density fixed to the nominal value and obtain a best-fit photon index of $\Gamma = 1.0 \pm 0.3$ and a 2−10 keV flux of $F = 6.6(5.6\text{–}7.2) \times 10^{-13}$ erg cm^{-2} s^{-1}. The magnitude of this flux falls within $\sim 2\sigma$ of the value obtained a year later using *NuSTAR* data (see Table 1) but notably ∼4 times less

Table 1
Spectral Results for XMMU J183245−0921539

Data Set (Fitted Band, Observation date)	N_H (10^{22} cm^{-2})	Γ	Flux[a] *XMM-Newton* (EPIC-PN) (EPIC MOS)	Flux[a] *Chandra* (ACIS)	Flux[a] *NuSTAR* (FPMA) (FPMB)	χ^2_ν (dof)
XMM-Newton (2−8 keV, 2011 March 13)	9.5[b]	1.0 ± 0.3	6.6(5.6–7.2) 6.4(5.4–7.1)	⋯	⋯ ⋯	0.97(41)
Chandra (2−8 keV, 2015 July 6)	9.5[b]	1.7 ± 0.5	⋯	7.7(6.1–8.5)	⋯	0.81(16)
NuSTAR (3−30 keV, 2016 March 21)	9.5[b]	1.5 ± 0.1	⋯	⋯	9.6(9.1–10.0) 9.7(9.3–10.1)	1.0(151)
Chandra + *XMM-Newton* (2−8 keV)[c]	9.7 ± 5	1.2 ± 0.7	6.2(2.6–6.7) 5.9(2.6–6.4)	8.9(3.8–9.5)	⋯	1.0(57)
XMM-Newton + *Chandra* + *NuSTAR* (2−30 keV)[c]	9.5 ± 2	1.5 ± 0.1	5.8 ± 0.5 5.2 ± 0.6	8.0 ± 0.8	9.4(9.0–9.8) 9.6(9.1–10.0)	1.0(112)

Notes.
[a] Absorbed flux for the 2–10 keV band in units of 10^{-13} erg cm^{-2} s^{-1}. Uncertainties are estimated using the XSPEC *flux* command for the 90% confidence level.
[b] Column density is fixed to the best-fit value obtained from a simultaneous spectral fit to the combined *XMM-Newton* + *Chandra* + *NuSTAR* data. Errors are given for 2 interesting parameters at the 90% C.L.
[c] We linked column density and photon index between the different spectra.

than that reported in Eger et al. (2016).[12] As a check, we entered the derived count rates and spectral parameters into PIMMS,[13] allowing for the 4.9% deadtime in the ACIS 1/8 sub-array observing mode. This verified the flux result presented here.

For the *XMM-Newton* analysis, we extracted EPIC-PN and MOS spectra using a $r = 30''$ aperture around XMMJ183245. Background spectra were extracted from an annulus region around the source. A joint fit to the PN and merged MOS spectra in the 2−8 keV band with the nominal absorbed power-law model yielded a photon index of $\Gamma = 1.0 \pm 0.3$ and a 2−10 keV flux $F = 6.6(5.6–7.2) \times 10^{-13}$ erg cm^{-2} s^{-1} for the EPIC-PN spectra and a similar yield for the MOS fits, with a fit statistic of $\chi^2_\nu = 0.97$ for 41 DoF, confirming the results of Abramowski et al. (2015).

We use the 2016 *NuSTAR* flux measurements, along with the corrected 2015 *Chandra* results and the 2011 *XMM-Newton* data, to quantify the source variability of XMMJ183245. Figure 4 summarized its flux and spectral history. The most extreme change is between the initial and latest data sets, representing a ∼50% fractional increase in flux, significant at the 5σ level. The power-law photon indices are found to be consistent between observations to within the measured errors.

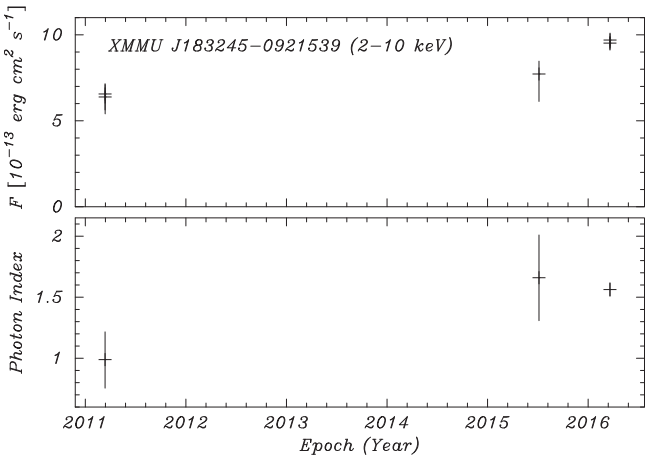

Figure 4. Best-fit 2–10 keV absorbed fluxes (top) and X-ray power-law photon indices (bottom) for XMMJ183245 obtained from the *XMM-Newton*, *Chandra*, and *NuSTAR* observations. The quoted errors are for the 90% confidence level. Data points are from Table 1.

4. Timing Analysis of XMMU J183245−0921539

We searched for temporal evidence of a binary orbit for XMMJ183245 using the *XMM-Newton*, *Chandra*, and *NuSTAR* data sets. Photon arrival times obtained from each mission were first corrected to the solar system barycenter using the JPL DE200 planetary ephemeris and the *Chandra* derived coordinates of R.A. 18:32:45.158, decl. −09:21:54.78 (J2000). Initial analysis shows no signature characteristic of an accreting system; the light curves are stable on all timescales and their fast Fourier transform (FFT) power spectra show no evidence of red noise. To search for a coherent pulsed signal we used both the FFT method and the unbinned Z^2_n test, for $n = 1$, 2, 3, 5, and the H-test, to be sensitive to both broad and narrow pulse profiles.

From the *Chandra* data we extracted $N = 399$ counts in a $r < 1\farcs8$ radius aperture, containing essentially no background contamination (⩽1 count). We performed a Nyquist-limited FFT search in the 0.3−10 keV energy band and found no significant signal for periods between 1.68 s and 10.4 ks, with a 3σ upper limit on a sinusoidal pulse fraction of $f_p(3\sigma) < 40\%$ for 2^{15} trials. For the *XMM-Newton* observation we obtained 576 cts and 830 cts from the merged MOS and the pn data sets, respectively, extracted using a $r < 0\farcs4$ source aperture in the 0.3−10 keV energy range. A 2^{16} element FFT search of the MOS data yields no significant signal, with an upper limit of $f_p(3\sigma) < 46.5\%$ for $0.6 < P < 8,310$ s. Similarly, from the pn data we obtain an $f_p(3\sigma) < 36.9\%$ between $P = 146.8$ ms and $P = 7.5$ ks using a 2^{18} element FFT. These upper limits take into account the estimated background contamination in the source aperture. We find no evidence for a binary orbit signature in any of these searches.

[12] We note that we obtain a similar number of extracted counts (409 cts, $0.3 < E < 10$ keV) for our spectrum as recorded by Eger et al. (2016) in their Table 1 (416 cts).
[13] http://cxc.harvard.edu/toolkit/pimms.jsp

The high time resolution *NuSTAR* data allow a search for coherent pulsations, as suggested by the X-ray spectrum of XMMJ183245, typical of a young, rapidly rotating pulsar, possibly associated with a HESS source. From the merged FPM data we extracted $N = 6030$ cts contained within a $r < 0.'8$ radius source aperture in the full *NuSTAR* energy band. For a 2^{27} element FFT we obtain an upper limit on the pulse fraction to $f_p(3\sigma) < 19.4\%$ between $P = 4$ ms and $P = 85.7$ ks, after allowing for the source aperture background. We also searched for a signal over a restricted energy range of <20 keV and 20−79 keV, however, none was detected. We repeated all our searches using the Z_n^2 method and H-test, which produce consistent results.

For the long time span (171 ks) of the *NuSTAR* observation we performed an additional test using an accelerated FFT search to sample a range of frequency derivatives typical of a energetic pulsar. In no case did we detect a significant pulsar or orbital signal. On the other hand, unlike for the *Chandra* and *XMM-Newton* data, the strong signature in the power spectrum at the 97-minute *NuSTAR* spacecraft orbital period and its many harmonics can mask an adjacent binary signal in the frequency domain. The non-detection of X-ray pulsation is common for gamma-ray binaries with upper limits on the pulsed fraction from ∼8% to 35%, since the unpulsed wind emission may be dominant (Hirayama et al. 1999; Martocchia et al. 2005; Rea et al. 2010, 2011; Rea & Torres 2011).

5. Spectral Analysis of N1, N2, N3

To determine the possible nature of the three X-ray sources detected in the hard band, N1, N2, and N3, we extracted *NuSTAR* and *XMM-Newton* spectra, using a $r = 30''$ aperture. The *Chandra* observation of XMMJ183245 was operated in the 1/8 sub-array mode and did not overlap any of these sources in its restricted field of view. Due to the lack of sufficient counts in the MOS spectra for spectroscopy, after background subtraction we only fit the EPIC-PN data. The *NuSTAR* FPMA data for N2 are heavily contaminated by additional stray-light background photons from a nearby bright source, and are excluded from the analysis. We again generated *NuSTAR* background spectra for each source using the `nuskybgd` model. The previous *XMM-Newton* background spectra proved adequate for their spectral analysis. After rebinning the spectra with at least 20 counts per bin, spectral fitting was performed from ∼3 keV to 20 keV where the background is not significant.

Given that we find no significant flux deviation between the *XMM-Newton* and *NuSTAR* observations for the three hard X-ray sources, we jointly fit the *XMM-Newton* and *NuSTAR* spectra for each. The fit results obtained for an absorbed power-law model are summarized in Table 2 and Figure 5. In addition, we fit an absorbed, optically thin thermal plasma model (`tbabs*apec`). We fixed the abundance to solar, since it is poorly constrained due to the absence of apparent Fe lines.

A power-law model fit to the *NuSTAR* + *XMM-Newton* spectra of N1 yields $N_{\rm H} = 17^{+10}_{-7} \times 10^{22}\,{\rm cm}^{-2}$ and a photon index $\Gamma = 2.1^{+0.5}_{-0.4}$. An absorbed optically thin thermal plasma model (`tbabs*apec`) fits the spectra equally well with $\chi^2_\nu = 1.0$, with a best-fit column density and temperature of $N_{\rm H} = (17^{+9}_{-7}) \times 10^{22}\,{\rm cm}^{-2}$ and $kT = 13^{+16}_{-5}$ [keV]. In contrast, *NuSTAR* + *XMM-Newton* spectra of N2 and N3 fit to a power-law model with harder power-law photon indices $\Gamma = 1.2 \pm 0.4$ and $\Gamma = 0.9^{+0.4}_{-0.3}$, respectively. An absorbed APEC model fit yields $kT = 46^{+18}_{-26}$ keV ($\chi^2_\nu = 0.57$) and 27^{+37}_{-12} keV ($\chi^2_\nu = 1.00$) for N2 and N3, respectively.[14] We also added a partial-covering absorption model (`pcfabs`) in order to account for X-ray reflection from the white dwarf surface or absorption in the accretion curtain for intermediate polars (Hailey et al. 2016). A `tbabs*pcfabs*apec` model fit did not constrain the parameters well for N2. The same model fit to the *NuSTAR* + *XMM-Newton* spectra of N3 ($\chi^2_\nu = 0.66$) yields a lower temperature $kT = 13^{+5}_{-3}$ keV, partial-covering column density N_H (pc) $= 10^{+5}_{-3} \times 10^{23}\,{\rm cm}^{-2}$ and covering factor $f_c = 0.88^{+0.05}_{-0.08}$.

Table 2
NuSTAR and *XMM-Newton* Spectral Fitting Results for the Three X-Ray Sources

Parameters	N1	N2	N3
XMM-Newton	J183239.7	J183250.1	J183314.2
counterpart	−091610	−091401	−092109
$N_{\rm H}[10^{22}\,{\rm cm}^{-2}]$	17^{+10}_{-7}	11^{+7}_{-5}	6^{+8}_{-4}
Γ	$2.1^{+0.5}_{-0.4}$	1.2 ± 0.4	$0.9^{+0.4}_{-0.3}$
Flux (2–20 keV)[a]	$3.7^{+1.5}_{-0.8}$	$4.1^{+0.8}_{-0.6}$	$4.2^{+0.7}_{-0.5}$
χ^2_ν (dof)	0.97 (34)	0.62 (18)	0.97 (28)

Note.
[a] Unabsorbed flux [10^{-13} erg cm^{-2} s^{-1}].

6. Discussion

6.1. X-Ray Emission from Gamma-Ray Binary Candidate HESS J1832−093

The X-ray spectral and timing signatures of HESS J1832−093—i.e., (1) a single power-law spectrum up to 30 keV, (2) with a photon index $\Gamma \approx 1.5$, (3) evidence for X-ray flux variation over time, and (4) a flat power-density spectrum without red noise—are consistent with the class of known TeV gamma-ray binaries (Dubus 2013), suggesting that it is a non-accreting NS binary system. Between a neutron star and its high-mass companion star, high-energy emission originates from the shocked region where the stellar and pulsar winds collide with each other (Dubus et al. 2015). In this scenario, X-rays stem from synchrotron radiation from accelerated electrons, while inverse Compton scattering of UV photons from a massive star are responsible for gamma-rays up to the TeV band. The non-detection of a spectral break is consistent with this picture where the synchrotron cutoff is expected to be at much higher energy $750(B\,[{\rm G}])^{-1}(d/0.1\,{\rm au})^2$ keV for typical ranges of the magnetic field strength in the pulsar wind (B) and the binary separation (d) (Dubus 2013). On the other hand, accreting NS-HMXBs normally show a spectral break at $E \sim 10$–20 keV (Coburn et al. 2002).

The 2−10 keV luminosity ($L_X = 2.3 \times 10^{33}$ erg s^{-1}), assuming that the source is associated with the GLIMPSE9 stellar cluster and SNR G22.7−0.2 at ∼4 kpc (Messineo et al. 2010; Su et al. 2014), is similar to HESS J0632+057 ($L_X \sim 10^{33}$ erg s^{-1}), while other gamma-ray binaries are brighter in the X-ray band by an order of magnitude. As Eger et al. (2016) pointed out, HESS J1832−093 and HESS J0632+057 possess similar characteristics, such as the faint X-ray

[14] The upper bound of plasma temperature is set by the maximum value ($kT = 64$ keV) allowed in the APEC model.

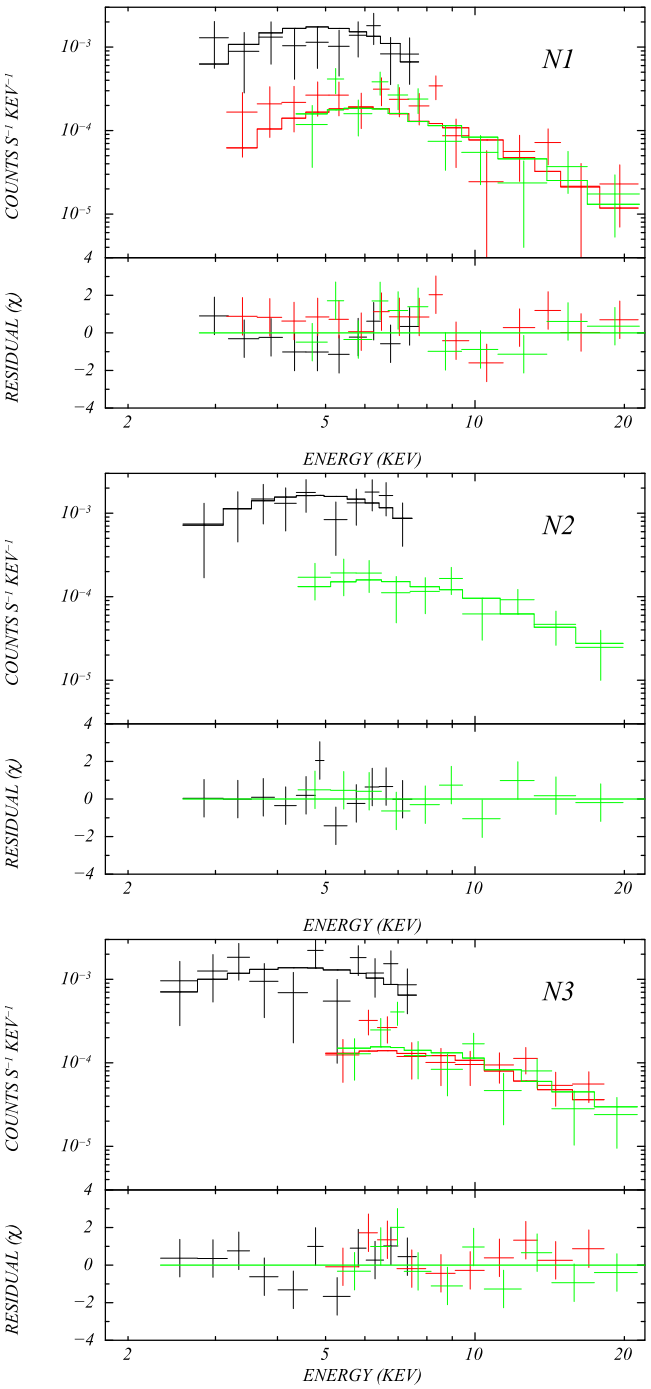

Figure 5. *XMM-Newton* + *NuSTAR* spectra of the three hard X-ray sources (EPIC-PN: black; module A: red; module B: green) jointly fit by an absorbed power-law model.

emission, the lack of *Fermi* GeV gamma-ray detection, and the spectral energy distribution over the X-ray and TeV gamma-ray bands. Further comparison with HESS J0632+057, as well as various emission models, is not viable until an orbital period is discovered and the high-energy emission is fully characterized in different orbital phases. As a TeV binary, HESS J1832−093 can be expected to exhibit X-ray flares similar to other gamma-ray binaries. For example, HESS J0632+057 displays $\gtrsim 5\times$ X-ray flux enhancement within <1 month (Bongiorno et al. 2011). *Swift* monitoring of XMMJ183245 over a year may have a good chance of detecting its orbital period.

6.2. IR Counterpart of XMMU J183245−0921539

In all TeV gamma-ray binaries, the IR and optical emission is predominantly from their massive companion stars (Dubus 2013). In the case of HESS J1832−093, the IR source 2MASS J18324516-0921545 with the magnitudes $J = 15.521 \pm 0.061$, $H = 13.264 \pm 0.036$, and $K = 12.172 \pm 0.019$ coincides with the *Chandra* position of XMMJ183245 (Cutri et al. 2003; Eger et al. 2016). According to the VizieR catalog, other IR surveys detected remarkably similar IR magnitudes: UKIDSS ($J = 15.359 \pm 0.005$, $H = 13.316 \pm 0.002$ and $K = 12.118 \pm 0.002$) and DENIS ($J = 15.326 \pm 0.18$ and $K = 12.080 \pm 0.16$) (Lucas et al. 2008). The weak variability of IR magnitudes such as $\Delta J \approx 0.2$, $\Delta H \approx 0.05$, and $\Delta K \approx 0.09$ is a common signature of HXMBs (Reig & Fabregat 2015). The GLIMPSE survey detected mid-IR emission (G022.4768−00.1539) at magnitudes 11.393 ± 0.047 (3.6 μm), 11.161 ± 0.068 (4.5 μm), 11.056 ± 0.090 (5.8 μm), and 10.779 ± 0.092 (8.0 μm). Both the large mid-IR brightness and colors suggest that the IR source is not an AGN (Stern et al. 2005; Mendez et al. 2013).

Given the IR magnitudes measured by 2MASS, we attempt to speculate the stellar type. Galactic hydrogen column density ($N_{\rm H} = 1.7 \times 10^{22}\,{\rm cm}^{-2}$) to XMMJ183245 estimated by radio surveys (Willingale et al. 2013) leads to the optical extinction $A_V = 7.7$ using the relation $N_{\rm H} = 2.2 \times 10^{21} A_V\,{\rm cm}^{-2}$ (Güver & Özel 2009). The higher hydrogen column density ($N_{\rm H} = 1 \times 10^{23}\,{\rm cm}^{-2}$) derived from fitting X-ray spectra indicates that this value is a lower limit of the optical extinction, since there may be additional dust absorption from a surrounding molecular cloud. Using the extinction ratios from Fitzpatrick & Massa (2009), we correct the IR magnitudes to $A_J = 2.05$ and $A_K = 0.87$. Assuming the source distance of 4.4 kpc, we derive absolute magnitudes of $M_J = 0.03$ and $M_K = -1.99$, leading to the spectral types B8V and B1.5V, respectively (Pecaut & Mamajek 2013). The mismatch in the stellar types derived from the J and K magnitudes may be due to an infrared excess primarily in the K band (thus it may account for the detection of mid-IR emission) from warm dust or bremsstrahlung from the stellar winds. If the optical extinction is higher than $A_V = 7.7$ due to local dust absorption, the IR magnitudes will be larger, thus it suggests a more massive O star. However, as demonstrated for identifying hard X-ray sources discovered by *INTEGRAL* (Nespoli et al. 2008; Coleiro et al. 2013), IR spectroscopy is required to determine the exact type of a companion star associated with XMMJ183245.

6.3. The Nature of the Field Sources N1, N2, N3

Hard X-ray detection of the three X-ray sources (N1, N2, and N3) points toward X-ray binaries harboring neutron star or black hole magnetic CVs or pulsars as demonstrated by *NuSTAR* studies of Galactic point sources (Hong et al. 2016; Fornasini et al. 2017) and serendipitous hard X-ray sources (Tomsick et al. 2017). The *XMM-Newton* counterparts of the three hard X-ray sources are consistent with point sources and their spatial extents are constrained to $\lesssim 10''$. In addition, there are about a dozen unidentified *XMM-Newton* sources in the region. Nearby H II regions and young stellar cluster GLIMPSE9 (Messineo et al. 2010) may account for a large number of X-ray sources. Alternatively, some of these X-ray sources may represent point-like diffuse X-ray emission, since

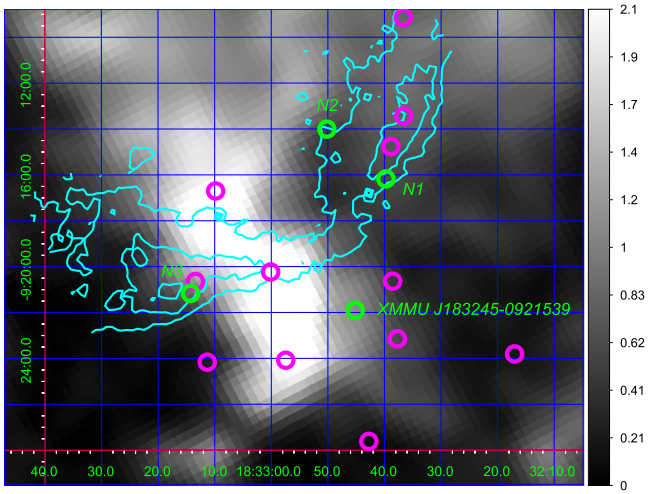

Figure 6. ^{13}CO molecular line map at $v = 75$ km s^{-1} around the southern region of the SNR G22.7−0.2 shell (Su et al. 2014). XMMJ183245 and the three hard X-ray sources (N1, N2, and N3) detected by *NuSTAR* in green circles are overlaid, while other *XMM-Newton* sources from the 3XMM catalog (Rosen et al. 2016) are indicated by magenta circles. Radio contours tracing the SNR G22.7−0.2 shell are shown in cyan.

they are located at the southern boundary of the G22.7−0.2 radio shell interacting with the molecular clouds (Su et al. 2014) (see Figure 6). Fast-moving supernova fragments in a dense molecular cloud can produce compact diffuse X-ray emission features, as observed in SNR IC 443 (Bykov et al. 2005).

The three hard X-ray sources N1, N2, and N3 exhibit rather distinct *NuSTAR* spectra (Table 1). They have 2–10 keV fluxes $\sim 4 \times 10^{-13}$ erg cm^{-2} s^{-1} (unabsorbed) corresponding to the X-ray luminosity $\sim 6 \times 10^{32}$ erg s^{-1} assuming that these sources are associated with the SNR G22.7−0.2, H II region, and GLIMPSE9 stellar cluster whose distances are 4.2–4.4 kpc (Messineo et al. 2010; Su et al. 2014). Below we discuss potential identification of the three *NuSTAR* sources, largely based on the *NuSTAR* results.

Source N1 (XMMU J183239.7−091610)—Among the three *NuSTAR* sources, N1 exhibits the softest X-ray spectra, with a power-law photon index $\Gamma = 2.1^{+0.5}_{-0.4}$. Spectral fitting with the thermal APEC model yields $kT \sim 13$ keV. A lack of bright IR counterparts ($K < 17$) within the *XMM-Newton* position error circle indicates that N1 is either a LMXB or magnetic CV if it is a binary system. Another possibility is a pulsar, in which case we expect no X-ray variability over time. However, given the large X-ray flux errors from the previous X-ray observations, it is unclear whether this source is variable or not.

Source N2 (XMMU J183250.1−091401)—The hard X-ray spectrum with $\Gamma = 1.2 \pm 0.4$ favors a NS-HMXB since NS-HMXBs generally have hard X-ray spectra with $\Gamma \sim 1$. The presence of the gamma-ray binary HESS J1832−093 and the nearby star cluster GLIMPSE9 suggests that some of the X-ray sources in the region may be HMXBs. Alternatively, N2 may be an intermediate polar since the best-fit plasma temperature is higher than ∼30 keV. There is an IR source with $K = 14.9$ located within 1.″3 from the *XMM-Newton* position. Following the corrections on IR magnitudes applied to XMMJ183245 (§6.2), this IR source is likely a B9V star or a more massive star. A better X-ray source localization with *Chandra* is crucial to determine its IR counterpart, then follow-up IR spectroscopy can identify the companion star type.

Source N3 (XMMU J183314.2−092109)—The *NuSTAR* source N3 may represent compact diffuse X-ray emission from the SNR-cloud interaction since it is located at the southern region of the G22.7−0.2 shell intersecting with molecular cloud G22.6−0.2, and its *NuSTAR* + XMM-Newton spectra fit to a hard power-law spectrum ($\Gamma \approx 1$). At the *NuSTAR* position of N3, there are two *XMM-Newton* sources separated by ∼20″. It is unclear whether N3 is an extended source overlapping the two *XMM-Newton* sources or truly a point source. There are several *XMM-Newton* sources overlapping with the strong ^{13}CO line emission region. Such X-ray morphology is similar to that of another middle-aged SNR IC 443 ($\tau \sim 3 \times 10^4$ years) harboring a prominent SNR-cloud interaction site with a dozen X-ray sources (Bocchino & Bykov 2003).

In IC 443, *Chandra* resolved one of the X-ray sources with a hard power-law spectrum ($\Gamma \approx 1$) to an extent of $r \sim 30''$, and it was interpreted as an SN ejecta fragment interacting with dense clouds (Bykov et al. 2005). Alternatively, shocked molecular clumps can emit X-rays with a hard spectrum at a SNR-cloud interaction site such as γ Cygni (Uchiyama et al. 2002). However, this scenario is unlikely since it predicts a more extended X-ray emission (∼a few arcmin) than the size (∼20″ or less) of the hard X-ray emission observed in IC 443 and N3 (Bocchino & Bykov 2003).

If N3 is an SN ejecta fragment similar to that in IC 443, its X-ray luminosity ($L_X \sim 10^{32}$ erg s^{-1}) indicates that the ejecta mass is likely $\gtrsim 10^{-2}\,M_\odot$ (Bykov et al. 2005). Given the radius (∼18 pc) and age ($\sim 3 \times 10^4$ years) of the SNR (Su et al. 2014), the estimated velocity (∼500 km s^{-1}) of a SN fragment at the SNR shell is large enough to produce the observed X-ray flux similar to the diffuse X-ray features observed in IC 443 (Bykov et al. 2005). The angular size of such an SN fragment is expected to be ∼10″ at the distance of G22.7−0.2 or less extended if the ejecta mass is smaller. Follow-up *Chandra* observations are warranted to resolve such small-scale features. Further *XMM-Newton* observations, improving the photon statistics, may detect Fe emission line from metal-rich SN ejecta as predicted by Bykov (2002). On the other hand, if N3 is indeed a point source, its hard X-ray spectra with $kT \approx 30$ keV (APEC model) and $kT \approx 13$ keV (partially covered APEC model) suggest an intermediate polar.

7. Summary

(1) An 87 ksec *NuSTAR* observation obtained high-quality X-ray spectra and timing data on XMMU J183245−0921539, the likely counterpart to the new gamma-ray binary candidate HESS J1832−093.

(2) The non-thermal X-ray spectrum of HESS J1832−093 extends up to at least ∼30 keV, with a power-law index of $\Gamma = 1.5$. No spectral break was observed. We found that the *NuSTAR* 2-10 keV flux is higher than that of the 2011 *XMM-Newton* observation by a factor of $1.5^{+0.4}_{-0.2}$ (90% c.l).

(3) No rapid X-ray pulsation indicative of a pulsar or slow modulation from a binary system were detected from XMMU J183245−0921539. The flat power-density spectrum shows no evidence of accretion.

(4) *NuSTAR* hard X-ray emission is detected from three *XMM-Newton* sources located within the radio shell of SNR G22.7−0.2. Broadband X-ray spectroscopy with

NuSTAR and *XMM-Newton* data suggests that one of these hard sources may be a supernova ejecta fragment interacting with a dense cloud, while the other two sources are likely X-ray binaries or magnetic CVs. A follow-up *Chandra* observation is required to identify their IR counterparts and resolve their spatial extents to smaller than $\sim 10''$ size.

In conclusion, the X-ray spectral and timing properties of HESS J1832−093 are similar to other gamma-ray binaries, especially HESS J0632-057. Detection of its orbital period, as well as simultaneous observations in the X-ray and gamma-ray bands, are the next steps to understanding the emission mechanism and geometry.

This work was supported under NASA Contract No. NNG08FD60C, and made use of data from the *NuSTAR* mission, a project led by the California Institute of Technology, managed by the Jet Propulsion Laboratory, and funded by the National Aeronautics and Space Administration. We thank the *NuSTAR* Operations, Software and Calibration teams for support with the execution and analysis of these observations. This research has made use of the *NuSTAR* Data Analysis Software (NuSTARDAS) jointly developed by the ASI Science Data Center (ASDC, Italy) and the California Institute of Technology (USA).

ORCID iDs

Kaya Mori https://orcid.org/0000-0002-9709-5389
E. V. Gotthelf https://orcid.org/0000-0003-3847-3957
Farid Rahoui https://orcid.org/0000-0001-7655-4120
John A. Tomsick https://orcid.org/0000-0001-5506-9855
Shuo Zhang https://orcid.org/0000-0002-2967-790X
Finn E. Christensen https://orcid.org/0000-0001-5679-1946
Fiona A. Harrison https://orcid.org/0000-0003-2992-8024
Daniel Stern https://orcid.org/0000-0003-2686-9241
William W. Zhang https://orcid.org/0000-0002-1426-9698

References

Abramowski, A., Acero, F., Aharonian, F., et al. 2015, MNRAS, 446, 1163
Aharonian, F., Akhperjanian, A. G., Aye, K.-M., et al. 2005, A&A, 442, 1
Aharonian, F., Akhperjanian, A. G., Bazer-Bachi, A. R., et al. 2006, A&A, 460, 743
Aharonian, F. A., Akhperjanian, A. G., Bazer-Bachi, A. R., et al. 2007, A&A, 469, L1
Albert, J., Aliu, E., Anderhub, H., et al. 2009, ApJ, 693, 303
Aliu, E., Archambault, S., Aune, T., et al. 2014, ApJ, 780, 168
An, H., Bellm, E., Bhalerao, V., et al. 2015, ApJ, 806, 166
An, H., Dufour, F., Kaspi, V. M., & Harrison, F. A. 2013, ApJ, 775, 135
Arnaud, K. A. 1996, in ASP Conf. Ser. 101, Astronomical Data Analysis Software and Systems V, ed. G. H. Jacoby & J. Barnes (San Francisco, CA: ASP), 17
Bocchino, F., & Bykov, A. M. 2003, A&A, 400, 203
Bongiorno, S. D., Falcone, A. D., Stroh, M., et al. 2011, ApJL, 737, L11
Bosch-Ramon, V., & Paredes, J. M. 2004, A&A, 417, 1075
Bykov, A. M. 2002, A&A, 390, 327
Bykov, A. M., Bocchino, F., & Pavlov, G. G. 2005, ApJL, 624, L41
Chernyakova, M., Neronov, A., Aharonian, F., Uchiyama, Y., & Takahashi, T. 2009, MNRAS, 397, 2123
Chernyakova, M., Neronov, A., Lutovinov, A., Rodriguez, J., & Johnston, S. 2006a, MNRAS, 367, 1201
Chernyakova, M., Neronov, A., & Walter, R. 2006b, MNRAS, 372, 1585
Coburn, W., Heindl, W. A., Rothschild, R. E., et al. 2002, ApJ, 580, 394
Coleiro, A., Chaty, S., Zurita Heras, J. A., Rahoui, F., & Tomsick, J. A. 2013, A&A, 560, A108
Cutri, R. M., Skrutskie, M. F., van Dyk, S., et al. 2003, The 2MASS All-Sky Catalog of Point Sources (Univ. Massachusetts and Infrared Processing and Analysis Center, IPAC/California Institute of Technology), 2246, 0
de la Cita, V. M., Bosch-Ramon, V., Paredes-Fortuny, X., Khangulyan, D., & Perucho, M. 2017, A&A, 598, A13
Dubus, G. 2013, A&ARv, 21, 64
Dubus, G. 2015, CRPhy, 16, 661
Dubus, G., Lamberts, A., & Fromang, S. 2015, A&A, 581, A27
Eger, P., Laffon, H., Bordas, P., et al. 2016, MNRAS, 457, 1753
Fitzpatrick, E. L., & Massa, D. 2009, ApJ, 699, 1209
Fornasini, F. M., Tomsick, J. A., Hong, J., et al. 2017, ApJS, 229, 33
Güver, T., & Özel, F. 2009, MNRAS, 400, 2050
H.E.S.S. Collaboration, Abramowski, A., Aharonian, F., et al. 2015, A&A, 577, A131
Hailey, C. J., Mori, K., Perez, K., et al. 2016, ApJ, 826, 160
Harrison, F. A., Craig, W. W., Christensen, F. E., et al. 2013, ApJ, 770, 103
Helfand, D. J., Becker, R. H., White, R. L., Fallon, A., & Tuttle, S. 2006, AJ, 131, 2525
Hirayama, M., Cominsky, L. R., Kaspi, V. M., et al. 1999, ApJ, 521, 718
Ho, W. C. G., Ng, C.-Y., Lyne, A. G., et al. 2017, MNRAS, 464, 1211
Hong, J., Mori, K., Hailey, C. J., et al. 2016, ApJ, 825, 132
Kaspi, V. M., Tavani, M., Nagase, F., et al. 1995, ApJ, 453, 424
Kishishita, T., Tanaka, T., Uchiyama, Y., & Takahashi, T. 2009, ApJL, 697, L1
Li, J., Torres, D. F., Chen, Y., et al. 2011, ApJL, 738, L31
Lucas, P. W., Hoare, M. G., Longmore, A., et al. 2008, MNRAS, 391, 136
Lyne, A. G., Stappers, B. W., Keith, M. J., et al. 2015, MNRAS, 451, 581
Madsen, K. K., Harrison, F. A., Markwardt, C. B., et al. 2015, ApJS, 220, 8
Martocchia, A., Motch, C., & Negueruela, I. 2005, A&A, 430, 245
Mendez, A. J., Coil, A. L., Aird, J., et al. 2013, ApJ, 770, 40
Messineo, M., Figer, D. F., Davies, B., et al. 2010, ApJ, 708, 1241
Mori, K., Gotthelf, E. V., Dufour, F., et al. 2014, ApJ, 793, 88
Mori, K., Hailey, C. J., Krivonos, R., et al. 2015, ApJ, 814, 94
Nespoli, E., Fabregat, J., & Mennickent, R. E. 2008, A&A, 486, 911
Pecaut, M. J., & Mamajek, E. E. 2013, ApJS, 208, 9
Rea, N., & Torres, D. F. 2011, ApJL, 737, L12
Rea, N., Torres, D. F., Caliandro, G. A., et al. 2011, MNRAS, 416, 1514
Rea, N., Torres, D. F., van der Klis, M., et al. 2010, MNRAS, 405, 2206
Reig, P., & Fabregat, J. 2015, A&A, 574, A33
Romero, G. E., Torres, D. F., Kaufman Bernadó, M. M., & Mirabel, I. F. 2003, A&A, 410, L1
Rosen, S. R., Webb, N. A., Watson, M. G., et al. 2016, A&A, 590, A1
Sierpowska-Bartosik, A., & Torres, D. F. 2008, APh, 30, 239
Stern, D., Eisenhardt, P., Gorjian, V., et al. 2005, ApJ, 631, 163
Su, Y., Yang, J., Zhou, X., Zhou, P., & Chen, Y. 2014, ApJ, 796, 122
Takahashi, T., Kishishita, T., Uchiyama, Y., et al. 2009, ApJ, 697, 592
Takata, J., Tam, P. H. T., Ng, C. W., et al. 2017, ApJ, 836, 241
Tavani, M., Arons, J., & Kaspi, V. M. 1994, ApJL, 433, L37
Tomsick, J. A., Lansbury, G. B., Rahoui, F., Clavel, M., & Fornasini, F. M. 2017, ApJS, 230, 25
Uchiyama, Y., Takahashi, T., Aharonian, F. A., & Mattox, J. R. 2002, ApJ, 571, 866
Uchiyama, Y., Tanaka, T., Takahashi, T., Mori, K., & Nakazawa, K. 2009, ApJ, 698, 911
Verner, D. A., Ferland, G. J., Korista, K. T., & Yakovlev, D. G. 1996, ApJ, 465, 487
Wik, D. R., Hornstrup, A., Molendi, S., et al. 2014, ApJ, 792, 48
Willingale, R., Starling, R. L. C., Beardmore, A. P., Tanvir, N. R., & O'Brien, P. T. 2013, MNRAS, 431, 394
Wilms, J., Allen, A., & McCray, R. 2000, ApJ, 542, 914